Compositing Fullerene-Derived Porous Carbon Fibers with Reduced Graphene Oxide for Enhanced ORR Catalytic Performance

Zhimin He, Ziqian Guo, Kun Guo *, Takeshi Akasaka and Xing Lu *

State Key Laboratory of Materials Processing and Die & Mould Technology,
School of Materials Science and Engineering, Huazhong University of Science and Technology, 1037 Luoyu Road,
Wuhan 430074, China; zm_he@hust.edu.cn (Z.H.); mtnhgzq@163.com (Z.G.); akasaka@tara.tsukuba.ac.jp (T.A.)
* Correspondence: guok@hust.edu.cn (K.G.); lux@hust.edu.cn (X.L.)

Abstract: Compositing all-carbon materials with distinct dimensions and structures has demonstrated the great potential to bring synergistic promotion to individual components for the electrocatalytic activity of oxygen reduction reaction (ORR). Fullerene-derived porous carbon fibers (FPCFs) offer unique one-dimensional (1D) nanostructures with abundant defects and a large specific surface area while graphene features two-dimensional (2D) nanostructures with fast electron transfer. Both carbon materials are promising alternatives to Pt-based electrocatalysts for ORR. Herein, a novel hierarchical composite (FPCFs@rGO) composed of FPCFs and reduced graphene oxide (rGO) is constructed by sonication-assisted mixing and high-temperature pyrolysis. When tested as an electrocatalyst for ORR, the 1D/2D FPCFs@rGO composite presents significantly enhanced performance compared to each individual component, indicating an eminent synergistic effect between FPCFs and rGO. The improved ORR performance of FPCFs@rGO is attributed to the unique hierarchical structure with abundant structural defects, a large specific surface area, and high porosity.

Keywords: fullerene; rGO; porous carbon fibers; oxygen reduction reaction

1. Introduction

Oxygen reduction reaction (ORR) requires efficient electrocatalysts due to its sluggish kinetics and high overpotential [1,2]. Since the groundbreaking discovery of the remarkable activity of nitrogen-doped carbon nanotubes, carbon-based metal-free materials have been regarded as promising alternatives to noble metal-based catalysts (e.g., platinum-group metals) [3]. The great potential of all-carbon materials as high-performance electrocatalysts towards ORR are justified by their facile preparation, high flexibility and conductivity, tunable surface chemistry and architecture, and high earth abundance [4–6]. Despite these factors, the ORR performance of metal-free carbon electrocatalysts is still unsatisfactory and strategic enhancement of the catalytic activity of the pristine carbon matrix remains a big challenge.

Fullerenes, an important family of carbon materials, feature with a high-stress carbon skeleton, abundant pentagon carbon rings and a unique electronic structure [7–9]. Unfolding fullerene cages can generate a carbon matrix rich in topological defects and edges, which can impart fullerene-derived carbon with high ORR activity [10,11]. For instance, Mu et al. reported that KOH-etching and pyrolysis of C_{60} powder can produce pentagon defect-rich porous carbon, showing superior ORR activity to the graphite-derived carbon matrix prepared by the same procedure [12]. On the other hand, fullerene molecules are flexible building units to assemble various nanoarchitectures due to the intermolecular π–π interactions [13–15]. This fascinating merit enables the on-demand fabrication of fullerene structures of sophisticated morphology. After high-temperature calcination, the original

nanoarchitecture can be retained [16–18]. Meanwhile, abundant pores are generated in favor of the adequate accessibility of active sites and fast mass transfer.

Recently, several research groups, including us, have reported that well-designed fullerene-derived carbon nanomaterials exhibit great potentials for energy-themed applications [19–21]. For example, our previous study demonstrated that porous carbon fibers prepared by the pyrolysis of fullerene-derived fibrous crystals show inspiring ORR activity [22]. However, such ORR activity is still inferior to that of noble metal-based catalysts and other heteroatom-doped carbon materials. Among the reported strategies for the performance enhancement of all-carbon electrocatalysts, compositing carbon materials of distinct dimensions and structures have been demonstrated to promise a great efficacy to enable a synergistic effect to individual components [23–25]. This thus stimulates us to move one step further to enhance the ORR performance of fullerene-derived porous carbon fibers by compositing with another type of carbon materials.

In this study, a novel composite consisting of fullerene-derived porous carbon fibers (FPCFs) and reduced graphene oxide (rGO) is fabricated and tested as an ORR electrocatalyst. The composite results from the sonication-assisted mixing and high-temperature pyrolysis of in-house prepared fullerene carbon fibers and graphene oxide (GO). Detailed characterizations reveal that calcination at 900 °C leads to the generation of a hierarchical composite (FPCFs@rGO) with abundant pores, a high specific surface area, and rich defects. Electrochemical measurements of FPCFs@rGO further uncover a synergistic activity enhancement with a half-wave potential of 0.762 V, which is 38 and 131 mV higher than those of FPCFs and rGO, respectively. Moreover, FPCFs@rGO exhibits remarkable long-term stability and outstanding methanol tolerance, which surpass the commercial 20% Pt/C.

2. Materials and Methods

2.1. Chemicals and Reagents

C_{60} fullerene was synthesized via a direct current discharge method and was isolated by high-performance liquid chromatography. [26] *m*-xylene and isopropyl alcohol (IPA) were purchased from Sinopharm Chemical Reagent Beijing Co., Ltd. (Beijing, China). The Nafion ionomer solution (5 wt.%) was bought from Sigma-Aldrich. The graphite powder, potassium persulfate, phosphorus pentoxide, and commercial 20 wt.% Pt/C catalyst were obtained from Beijing InnoChem Science & Technology Co., Ltd. All the reagents mentioned above were used as received without further purification.

2.2. Synthesis of Graphene Oxide (GO)

In a typical process, 3 g of graphite powder, 2.5 g of $K_2S_2O_8$, and 2 g of P_2O_5 are dissolved in 20 mL of H_2SO_4 and then stirred at 80 °C for 4.5 h. When the sample was cooled down to ambient temperature, the slurry was diluted in 500 mL of deionized water and then stirred overnight. The pretreated mixture was filtered and dried at 80 °C, and then dispersed into 120 mL of H_2SO_4, into which 15 g of $KMnO_4$ was carefully added in an ice bath. Thereafter, the slurry was transferred to an oil bath and stirred for 2 h at 35 °C. After that, 250 mL of an ice-water mixture was carefully added into the slurry with the ice bath and stirred for another 2 h. Then, the slurry was transferred into a 1000 mL of beaker and was diluted with 700 mL of both H_2O and 30 mL of 30% H_2O_2 to produce a bright yellow product. The obtained slurry was centrifuged and washed with 1 L of diluted HCl $V_{H_2O} : V_{HCl} = 90 : 10$ and then washed with deionized water until the pH reached neutral. The dispersion was dialyzed for at least one week to remove residual impurities.

2.3. Synthesis of Fullerene Carbon Fibers (FCFs)

FCFs were prepared by a modified liquid–liquid interfacial precipitation (LLIP) method according to a previous report [27]. *m*-xylene and IPA were selected as good and poor solvents of C_{60}, respectively. Briefly, 10 mL of IPA was slowly injected into 5 mL of C_{60} m-xylene solution (2 mg mL^{-1}). Subsequently, the suspension was aged for 24 h at room

temperature. Finally, after evaporating the solvent and washing with IPA for three times, FCFs were finally obtained after drying at 60 °C under reduced pressure for 12 h.

2.4. Synthesis of FCFs Embedded in GO (FCFs@GO)

10 mg of GO was dispersed into 20 mL of IPA and ultrasonicated for 2 h, and 50 mg of FCFs was dispersed into 20 mL of IPA. Subsequently, the above two solutions were thoroughly mixed. FCFs@GO was obtained after centrifugation and vacuum drying for 12 h at 60 °C.

2.5. Synthesis of Reduced Graphene Oxide (rGO), Fullerene-Derived Porous Carbon Fibers (FPCFs), and FPCFs Composited with rGO (FPCFs@rGO)

The resulting GO, FCFs, and FCFs@GO were calcined at 900 °C for 2 h in an argon atmosphere at a ramp rate of 5 °C min^{-1}. The corresponding products are denoted as rGO, FPCFs, and FPCFs@rGO.

2.6. Materials Characterization

Scanning electron microscopy (SEM, Quanta 650 FEG, FEI), transmission electron microscopy (TEM, Tecnai G2 F30), and high-resolution TEM (HRTEM) were employed to observe the structure and morphology of the samples. In a typical sample preparation for TEM, 1 mg of the as-prepared sample was ultrasonically dispersed in 5 mL of ethanol and supernatant was then dropped onto the copper mesh. X-ray diffraction (XRD) patterns were collected on an Empyrean XRD diffractometer (Panalytical, Holland) at 40 kV and 40 mA with Cu Kα radiation, and the continuous scan mode with a scan speed of 10° min^{-1} was used. Raman spectra were recorded on a Bruker VERTEX 70 spectrometer with an Ar ion laser at an excitation wavelength of 532 nm. Nitrogen adsorption/desorption tests were conducted at the liquid nitrogen temperature of 77K on a Tristar II 3020 gas adsorption analyzer (Micromeritics, Norcross, GA, USA) after degassing under vacuum at 60 °C for 12 h using a sample degas system (Micromeritics VacPrep 061). The specific surface area (SAA) was calculated by the Brunauer–Emmett–Teller (BET) method using the adsorption branch in the relative pressure p/p$_0$ range of 0.05–0.30, whereas the pore size distribution was obtained by the Barrett–Joyner–Halenda (BJH) method. X-ray photoelectron spectroscopy (XPS) tests were performed on an AXIS-ULTRA DLD-600W instrument with a monochromatized Al Kα source. The purity of the as-synthesized C$_{60}$ fullerene was evaluated by the laser desorption/ionization time-of-light (LDI-TOF).

2.7. Electrochemical Tests

ORR measurements were performed in O$_2$ or N$_2$-saturated 0.1 M KOH. Prior to the test, the electrolyte solution was purged by high-purity (99.999%) O$_2$ for 30 min. Pt sheet and Hg/HgO were used as the counter electrode and reference electrode, respectively. In a typical process of preparing the catalyst ink, 5 mg of catalyst is dissolved in a mixture of 960 μL of ethanol and 40 μL of Nafion solution, and sonicated for 40 min. The homogeneous ink was then drop-casted onto glassy carbon electrodes with a mass loading of 0.25 mg cm^{-2}.

CV curves were recorded on a CHI 660E electrochemical workstation equipped with an electrode rotator (Pine Instrument) in a standard three-electrode cell at a sweep rate of 20 mV s^{-1} in O$_2$ or N$_2$-saturated 0.1M KOH solution. LSV curves were obtained at a scan rate of 10 mV s^{-1} and rotating speeds from 400 to 1600 rpm. Long-term stability measurements were conducted using the chronoamperometric technique at 0.6 V for 12 h. The methanol tolerance was investigated by adding methanol solution (3 M and 10 mL) during the i-t response tests. All the potentials have been referenced to the reversible hydrogen electrode (RHE) according to the following equations:

$$E(RHE) = E(Hg/HgO) + 0.059 \times pH + 0.098 \text{ V}$$

The transferred electron number was calculated according to the K-L equation as follows:

$$\frac{1}{J} = \frac{1}{B\omega^{1/2}} + \frac{1}{J_K} \tag{1}$$

$$B = 0.2nFC_0(D_0)^{2/3}v^{-1/6} \tag{2}$$

where J and J_K are the measured current density and kinetic current density, respectively. ω is the electrode rotating rates. n represents the transferred electron number per oxygen molecule, F is the faradaic constant (96485 C mol^{-1}), D_0 is the diffusion coefficient of O$_2$ in 0.1 M KOH (1.9×10^{-5} cm^2 s^{-1}), v is the kinetic viscosity of the electrolyte (0.01 cm^2 s^{-1}), and C$_0$ is the bulk concentration of O$_2$ in 0.1 M KOH (1.2×10^{-6} mol cm^{-3}).

3. Results and Discussion

SEM and TEM images of GO are shown in Figure 1(a1,b1). Typical morphology of GO with wrinkled and crimped two-dimensional sheets was observed [28]. A stacked graphite structure of a few GO sheets was further confirmed by an HR-TEM image (Figure 1(c1)). As shown in Figure 1(a2,b2), FCFs exhibits one-dimensional fibrous morphology. The HR-TEM image (Figure 1(c2)) further reveals its crystalline nature, which results from the ordered stacking of fullerene molecules. Figure 1(a3,b3) show that fullerene fibers are successfully embedded into graphene sheets. Furthermore, randomly entangled fullerene fibers mixed with GO lead to a hierarchical structure. The HR-TEM image (Figure 1(c3)) of FCFs@GO further confirms the co-existence of fullerene fibers and GO.
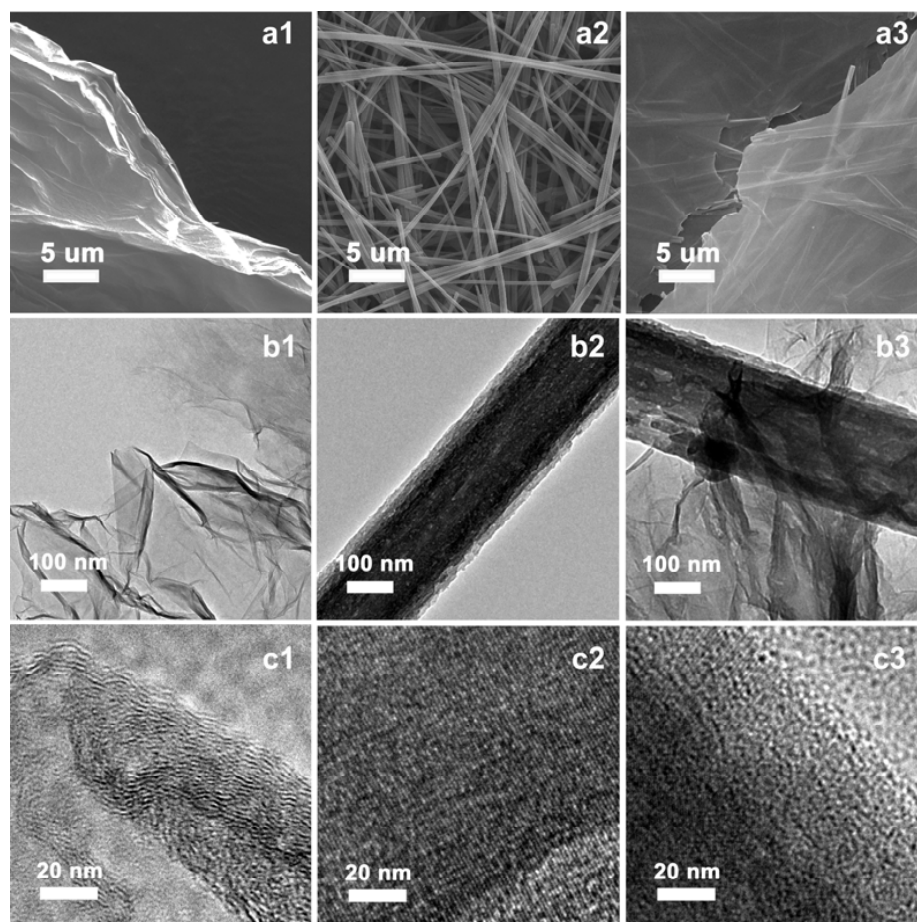
Figure 1. SEM, TEM, and HR-TEM images of GO (**a1**,**b1**,**c1**), FCFs (**a2**,**b2**,**c2**), and FCFs@GO (**a3**,**b3**,**c3**).

As shown in Figure 2(a1–c1), SEM, TEM and HR-TEM images reveal that high-temperature pyrolysis leads to a reduction of GO (rGO) and dense aggregation of graphite layers [29]. The SEM image (Figure 2(a2)) of FPCFs shows that the original fibrous morphology of FCFs is well-maintained after calcination. Furthermore, considerable mesopores can be observed on the fibrous structure in the TEM image (Figure 2(b2)). The HR-TEM image (Figure 2(c2)) indicates that FPCFs consist of randomly oriented graphitic domains, indicating its amorphous nature and defect-rich matrix. Figure 2(a3) shows that FPCFs@rGO has a similar morphology with FCFs@GO. The TEM image (Figure 2(b3)) shows that several graphene sheets are attached to the fibers and show low aggregation compared to rGO. Moreover, an amorphous carbon structure was also observed in the HR-TEM image of FPCFs@rGO (Figure 2(c3)).
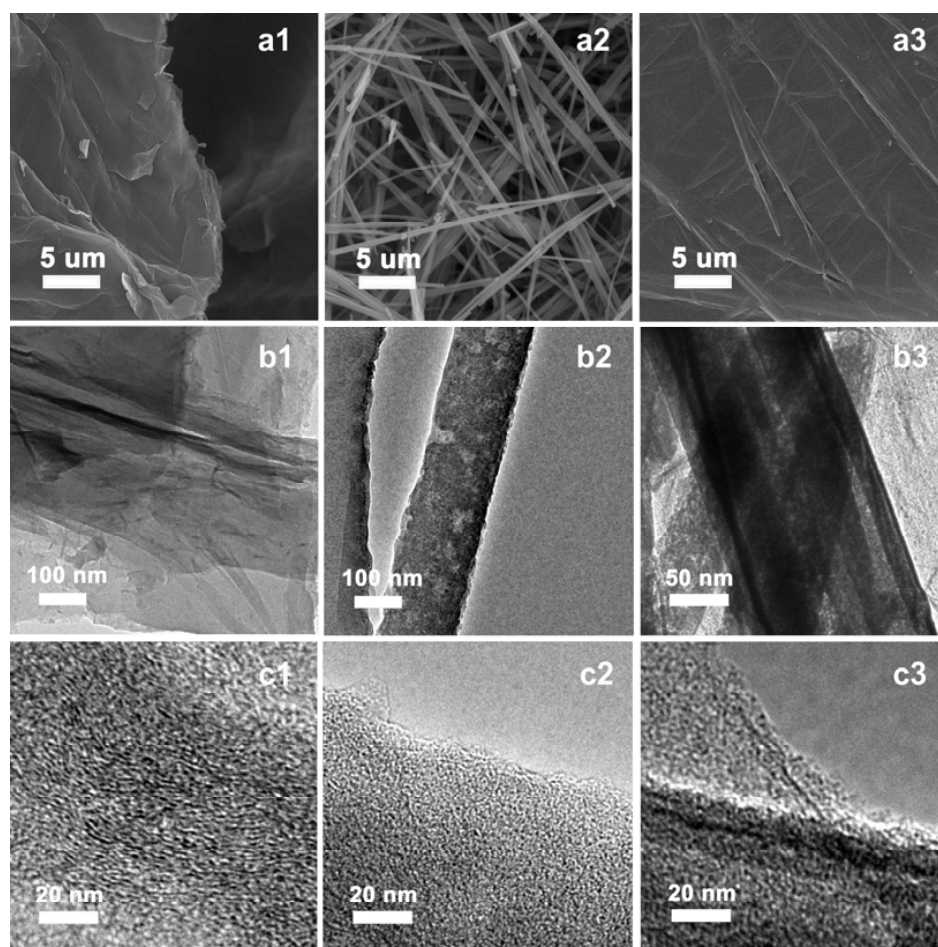
Figure 2. SEM, TEM, and HR-TEM images of rGO (**a1,b1,c1**), FPCFs (**a2,b2,c2**), and PNCFs@rGO (**a3,b3,c3**).

Figure 3a shows the powder XRD patterns of pristine C_{60} powder, GO, FCFs, and FCFs@GO. Intense peaks of pristine C_{60} powder indicate its crystalline nature. FCFs and FCFs@GO display similar XRD patterns, which result from the stacked fullerene molecules after self-assembly. The high purity of pristine C_{60} is clearly revealed in Figure S1. For GO, an intense peak at 11.2° originates from the stacking of graphitic layers. After pyrolysis, as displayed in Figure 3b, the diffraction peak at 25.7° emerges, which is indexed to the inter-plane (002) of graphite, confirming the reduction of GO. [30] For FPCFs and FPCFs@rGO, the sharp diffraction peaks of FCFs and FCFs@GO disappear, which are accompanied by peaks at around 24.3°, suggesting the decomposition of C_{60} molecules. Figure 3c shows the Raman spectra of pristine C60 powder, GO, FCFs, and FCFs@GO. For GO, two bands at around 1350 and 1594 cm^{-1}, corresponding to D and G bands, were observed. For

pristine C_{60} powder, FCFs, and FCFs@GO, typical Raman vibrations of C_{60} molecules were detected, again confirming the existence of C_{60}. [15] However, these peaks are replaced by D and G bands in both FPCFs and FPCFs@rGO, indicating the breaking of C_{60} carbon cages after pyrolysis. Furthermore, the intensity ratio of D and G bands for FPCFs@rGO is 1.06, higher than those of rGO and FPCFs, implying abundant structural defects in FPCFs@rGO.
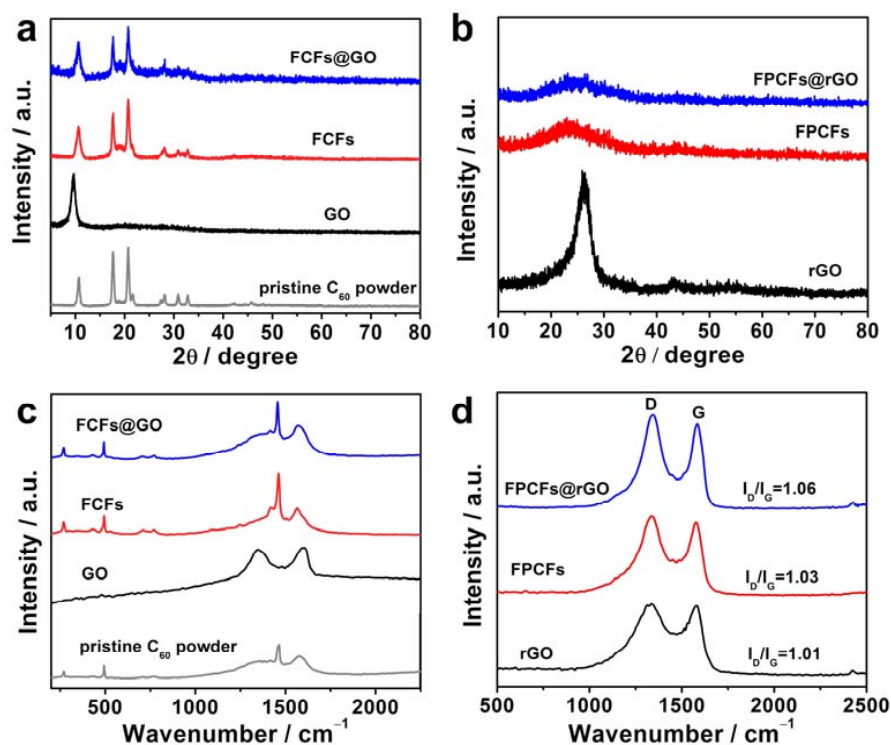

Figure 3. (**a**) XRD patterns and (**c**) Raman spectra of pristine C60 powder, GO, FCFs, and FCFs@GO. (**b**) XRD patterns and (**d**) Raman spectra of rGO, FPCFs, and FPCFs@rGO.

The SSA and pore structure of the as-prepared samples were studied by N_2-adsorption–desorption isotherms. As shown in Figure 4a, all samples exhibit type-IV isotherms. Despite this, rGO exhibits a small SSA ($76 \, m^2 \, g^{-1}$) and low porosity. Remarkably, FPCFs hold a more obvious hysteresis loop compared to rGO, indicating plenty of mesopores inside FPCFs, which is further confirmed by the pore size distribution curve (Figure 4b). Moreover, the SSA of FPCFs is $719 \, m^2 \, g^{-1}$, much larger than that of rGO. The large SSA and high porosity of FPCFs are ascribed to the decomposition of fullerene cages at high temperature, which are different from GO that is tightly stacked by π–π interaction after high-temperature treatment. Interestingly, FPCFs@rGO shows a higher N_2 adsorption plateau with a similar isotherm and has a larger SSA of $1017 \, m^2 \, g^{-1}$ compared to both rGO and FPCFs, indicating the significant enhancement of SSA and porosity by combining FPCFs with rGO.
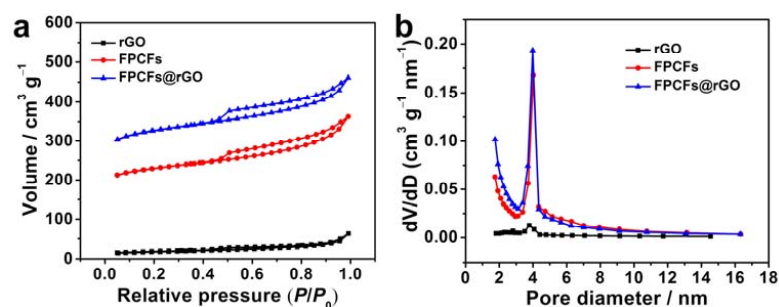
Figure 4. (**a**) Nitrogen adsorption–desorption isotherms and (**b**) pore size distributions of rGO, FPCFs, and FPCFs@rGO.

Chemical states of elements and surface compositions of the as-prepared samples were investigated by XPS measurements. Figure 5a reveals that the C 1s and O 1s peaks were detected in all samples. The high intensity of the O 1s peak is attributed to abundant O-related groups of GO (Table S1), which then are removed by the high-temperature pyrolysis (rGO exhibits low intensity of the O 1s peak). The HR-XPS spectra of the C 1s peak of all samples are shown in Figure 5b. The C 1s region of GO can be fitted into six peaks: C-sp^2 (C = C, 284.3 eV), C-sp^3 (C-C, 285.4 eV), C-O (epoxy and hydroxyl, 286.2 eV), C = O (carbonyl, 287.5 eV), C (= O)-(OH) (carboxyl, 289.2 eV), and π–π* satellite peak (290.6 eV). Obvious decreases of O-related peaks in rGO were detected, resulting in the dominant sp^2- and sp^3-C. It is not surprising that FCFs are entirely composed of sp^2-C as they are made up of sp^2-conjugated fullerene molecules. The decomposition of fullerene cages after high-temperature pyrolysis leads to an increase of the sp^3-C content in FPCFs. Similar results were obtained for FPCFs@rGO. Previous studies reported that the collapse of fullerene molecules can produce abundant structural defects (e.g., pentagon defects and edges). Furthermore, the sp^3-C to sp^2-C ratio (sp^3-C/sp^2-C) reflects the defect content in the carbon matrix and a high content of structural defects can deliver a high electrocatalytic activity. [31] Notably, FPCFs@rGO has a sp^3-C/sp^2-C ratio of 0.62, higher than those of rGO (0.44) and FPCFs (0.56), indicating a higher defect content in FPCFs@rGO. The increased sp^3-C content is due probably to the reconstruction and bonding between the fullerene-derived carbon matrix and rGO skeleton.
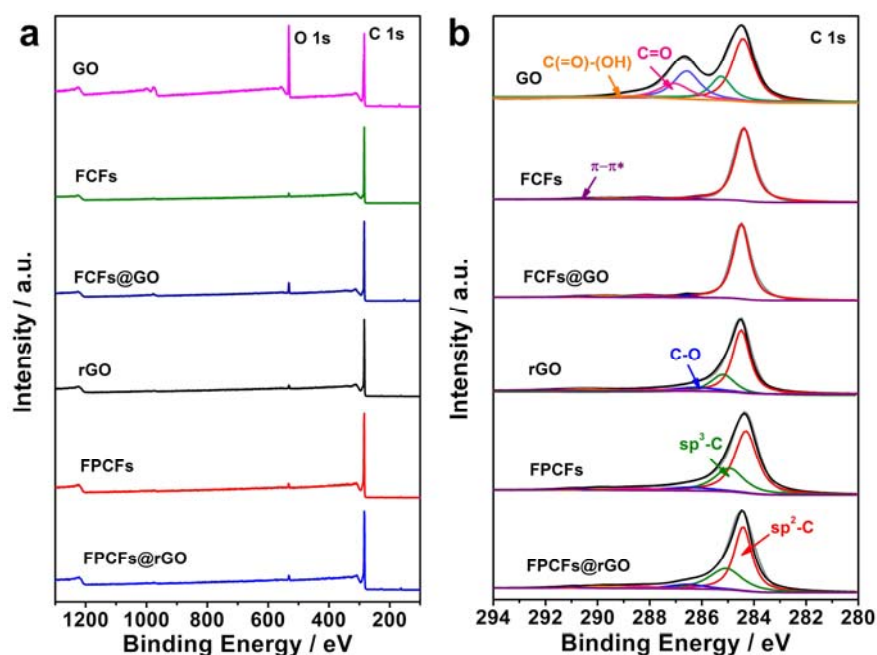
Figure 5. (**a**) Full survey XPS spectra and (**b**) high-resolution XPS spectra of C 1s of GO, FCFs, FCFs@GO, rGO, FPCFs, and FPCFs@rGO.

The ORR activities of rGO, FPCFs, FPCFs@rGO, and 20 wt.% Pt/C were evaluated by CV and LSV tests. Furthermore, the ORR activities of GO, FCFs, and FCFs@GO were also studied by LSV tests. As displayed in Figure S2, FCFs@GO shows an enhanced ORR activity compared to GO and FCFs, indicating an obvious contribution of such well-constructed nanoarchitecture to the catalytic activity. As shown in Figure 6a, CV curves of rGO, FPCFs, FPCFs@rGO, and 20 wt.% Pt/C show obvious oxygen redox peaks in 0.1 M O_2-saturated KOH media compared to those in N_2-saturated electrolytes, indicating that all samples exhibit decent ORR activity. The peak potential (E_p) of rGO is 0.612 V, whereas the E_p of FPCFs is 0.689 V, indicating a better ORR activity of FPCFs than rGO. Remarkably, FPCFs@rGO shows a more positive E_p value (0.742 V) compared to those of rGO and FPCFs, suggesting a significantly enhanced ORR activity of FPCFs@rGO. LSV curves

(Figure 6b) further confirm the ORR activity enhancements of FPCFs@rGO compared to rGO and FPCFs. FPCFs@rGO has an onset potential (E_0) of 0.895 V, a half-wave potential ($E_{1/2}$) of 0.762 V, and a limiting current density (J_L) of 4.96 mA cm^{-2}, which are much better than those of rGO (E_0 = 0.751 V, $E_{1/2}$ = 0.593 V, and J_L = 2.43 mA cm^{-2}) and FPCFs (E_0 = 0.874 V, $E_{1/2}$ = 0.724 V, and J_L = 4.51 mA cm^{-2}). Despite being inferior to 20 wt.% Pt/C, the ORR activities of FPCFs@rGO are still comparable or better compared to some recently reported carbon-based metal-free catalysts (Table S2). The corresponding Tafel plots fitted are displayed in Figure 6c. The Tafel slope of FPCFs@rGO is 75.9 mV dec^{-1}, smaller than that of rGO (105.1 mV dec^{-1}) and FPCFs (88.5 mV dec^{-1}), revealing the faster ORR kinetics and higher intrinsic catalytic activity of FPCFs@rGO. The superior ORR activity of FPCFs compared to rGO is attributed to abundant intrinsic structural defects derived from the fullerene cages decomposition as well as to the unique nanofiber structure with large SSA and abundant pores. The former offers plenty of edges and topological defects, thus providing a large number of active centers, while the latter ensures a sufficient exposure of active sites and a fast mass transfer during ORR. On one hand, the synergistic enhancement of FPCFs@rGO is undoubtedly linked to its unique hierarchical structure and substantial increase of both defect content and SSA. On the other hand, potential chemical bonding between the fullerene-derived carbon matrix and graphene skeleton in the resulting FPCFs@rGO, as disclosed by XPS results, may create additional active sites and thus contribute to the enhanced ORR activity.
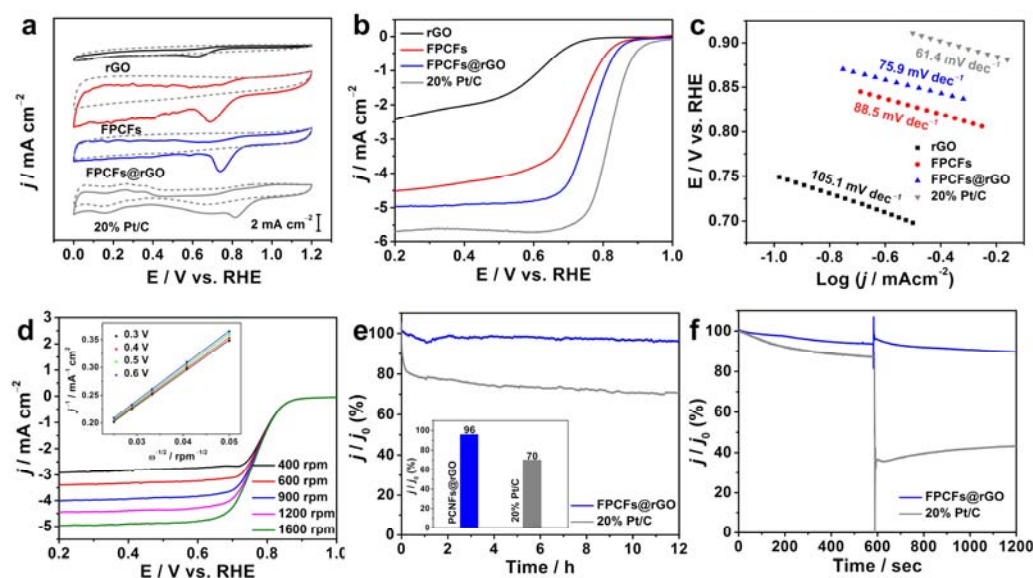
Figure 6. (**a**) CV curves, (**b**) LSV curves, and (**c**) Tafel plots of rGO, FPCFs, FPCFs@rGO, and 20 wt.% Pt/C. (**d**) LSV curves of FPCFs@rGO at a series of rotation rates from 400 to 2000 rpm with a scan rate of 10 mV s^{-1}. (**e**) Long-term durability (inset: comparison of current density after chronoamperometry) and (**f**) methanol immunity tests of FPCFs@rGO and 20 wt.% Pt/C.

A series of LSV curves of FPCFs@rGO recorded at different rotating speeds ranging from 400 to 1600 rpm are shown in Figure 6d. The J_L becomes larger with the increasing rotation rates in virtue of the decreased diffusion distance and the increased mass transfer rate of oxygen, reflecting a first-order reaction of ORR. The K-L plots of FPCFs@rGO at a series of potentials are illustrated in the inset of Figure 6d. The calculated average number of the electron transfer number (*n*) is 3.84, suggesting that FPCFs@rGO undergoes the four-electron reduction pathway during the alkaline ORR processes. However, the *n* values of rGO and FPCFs is 2.75 and 3.14 (Figure S3 and Figure S4), respectively, indicating the insufficient 4e reaction pathway.

The durability and methanol immunity of FPCFs@rGO were evaluated by chronoamperometry. For comparison, the commercial 20 wt.% Pt/C was also tested under the same

procedure. As displayed in Figure 6e, the commercial Pt/C exhibits an obvious decay of the current density at the beginning of the *i-t* response and the final current density retention is only 70% after 12 h of operation (inset of Figure 6e). On the contrary, FPCFs@rGO experiences a slight decay of 4% on the current density, demonstrating its remarkable long-term stability. Figure 6f presents the i-t response with methanol added in the middle of the measurements. FPCFs@rGO displays negligible decay on the current density after the methanol addition while the Pt/C catalyst goes through a steep drop, which indicates that FPCFs@rGO holds excellent immunity towards methanol. These results demonstrate that FPCFs@rGO possesses an enhanced catalytic activity, an outstanding stability, and a remarkable methanol tolerance, implying its great potential in energy-related applications.

4. Conclusions

In summary, we demonstrated that the ORR catalytic performance of fullerene-derived porous carbon fibers can be significantly improved by compositing with rGO (PCFs@rGO). The synergistic effect is testified by the better ORR activity of PCFs@rGO than that of both PCFs and rGO. The enhanced catalytic activity of PCFs@rGO is attributed to the increased surface area, porosity, and defect content, which enabled the densified active sites, improved the exposure of active sites, and promoted the efficiency of mass transfer during the ORR process. This work provides a useful strategy for promoting the catalytic activity of the pristine carbon matrix.

Supplementary Materials: The following are available online at https://www.mdpi.com/article/10.3390/c8010013/s1, Figure S1: LDI-TOF mass spectrum of the synthesized C_{60} fullerene, Table S1: Surface compositions of the as-prepared samples from XPS tests, Figure S2: LSV curves of GO, FCFs and FCFs@GO with an rotation speed of 1600 rmp at 10 mV s^{-1}, Figure S3: LSV curves at 10 mV s^{-1} and different rotation rates from 400 to 1600 rpm, and the corresponding K-L plots at different potentials of rGO (a) and FPCFs (b), Figure S4: Average electron transfer number of rGO, FPCFs and FPCFs@rGO, Table S2: Comparison of the ORR performance of FPCFs@rGO with recently reported metal-free catalysts in 0.1 M KOH solution.

Author Contributions: Conceptualization, Z.H.; methodology, Z.H. and Z.G.; writing—original draft preparation, Z.H.; writing—review and editing, K.G. and X.L.; supervision, X.L. and T.A. All authors have read and agreed to the published version of the manuscript.

Institutional Review Board Statement: Not applicable.

Informed Consent Statement: Not applicable.

Data Availability Statement: No new data were created or analyzed in this study. Data sharing is not applicable to this article.

Conflicts of Interest: The authors declare no conflict of interest.

References

1. Dai, L.; Xue, Y.; Qu, L.; Choi, H.-J.; Baek, J.-B. Metal-Free Catalysts for Oxygen Reduction Reaction. *Chem. Rev.* **2015**, *115*, 4823–4892. [CrossRef]
2. Chen, L.; Xu, X.; Yang, W.; Jia, J. Recent Advances in Carbon-based Electrocatalysts for Oxygen Reduction Reaction. *Chin. Chem. Lett.* **2020**, *31*, 626–634. [CrossRef]
3. Gong, K.; Du, F.; Xia, Z.; Durstock, M.; Dai, L. Nitrogen-Doped Carbon Nanotube Arrays with High Electrocatalytic Activity for Oxygen Reduction. *Science* **2009**, *323*, 760–764. [CrossRef] [PubMed]
4. Li, X.; Zhao, Y.; Yang, Y.; Gao, S. A Universal Strategy for Carbon–based ORR–active Electrocatalyst: One Porogen, Two Pore–creating Mechanisms, Three Pore Types. *Nano Energy* **2019**, *62*, 628–637. [CrossRef]

5.   Zhu, J.; Li, W.; Li, S.; Zhang, J.; Zhou, H.; Zhang, C.; Zhang, J.; Mu, S. Defective N/S-Codoped 3D Cheese-Like Porous Carbon Nanomaterial toward Efficient Oxygen Reduction and Zn–Air Batteries. *Small* **2018**, *14*, 1800563–1800572. [CrossRef] [PubMed]

6.   Liu, Q.; Wang, Y.; Dai, L.; Yao, J. Scalable Fabrication of Nanoporous Carbon Fiber Films as Bifunctional Catalytic Electrodes for Flexible Zn-Air Batteries. *Adv. Mater.* **2016**, *28*, 3000–3006. [CrossRef] [PubMed]

7.   Echegoyen, L.; Echegoyen, L.E. Electrochemistry of Fullerenes and Their Derivatives. *Acc. Chem. Res.* **1998**, *31*, 593–601. [CrossRef]

8.   Wang, Y.; Jiao, M.; Song, W.; Wu, Z. Doped Fullerene as a Metal-free Electrocatalyst for Oxygen Reduction Reaction: A First-principles Study. *Carbon* **2017**, *114*, 393–401. [CrossRef]

9.   Guldi, D.M. Fullerene–porphyrin Architectures; Photosynthetic Antenna and Reaction Center Models. *Chem. Soc. Rev.* **2002**, *31*, 22–36. [CrossRef] [PubMed]

10. Tan, Z.; Ni, K.; Chen, G.; Zeng, W.; Tao, Z.; Ikram, M.; Zhang, Q.; Wang, H.; Sun, L.; Zhu, X.; et al. Incorporating Pyrrolic and Pyridinic Nitrogen into a Porous Carbon made from C60 Molecules to Obtain Superior Energy Storage. *Adv. Mater.* **2017**, *29*, 1603414–1603422. [CrossRef] [PubMed]

11. Chen, X.; Chang, J.; Ke, Q. Probing the Activity of Pure and N-doped Fullerenes towards Oxygen Reduction Reaction by Density Functional Theory. *Carbon* **2018**, *126*, 53–57. [CrossRef]

12. Zhu, J.; Huang, Y.; Mei, W.; Zhao, C.; Zhang, C.; Zhang, J.; Amiinu, I.S.; Mu, S. Effects of Intrinsic Pentagon Defects on Electrochemical Reactivity of Carbon Nanomaterials. *Angew. Chem. Int. Ed.* **2019**, *58*, 3859–3864. [CrossRef]

13. Zheng, S.; Cuong, N.T.; Okada, S.; Xu, T.; Shen, W.; Lu, X.; Tsukagoshi, K. Solvent-Mediated Shape Engineering of Fullerene (C_{60}) Polyhedral Microcrystals. *Chem. Mater.* **2018**, *30*, 7146–7153. [CrossRef]

14. Shrestha, R.G.; Shrestha, L.K.; Khan, A.H.; Kumar, G.S.; Acharya, S.; Ariga, K. Demonstration of Ultrarapid Interfacial Formation of 1D Fullerene Nanorods with Photovoltaic Properties. *ACS Appl. Mater. Interfaces* **2014**, *6*, 15597–15603. [CrossRef]

15. Sathish, M.; Miyazawa, K.; Sasaki, T. Nanoporous Fullerene Nanowhiskers. *Chem. Mater.* **2007**, *19*, 2398–2400. [CrossRef]

16. Shrestha, L.K.; Shrestha, R.G.; Yamauchi, Y.; Hill, J.P.; Nishimura, T.; Miyazawa, K.i.; Kawai, T.; Okada, S.; Wakabayashi, K.; Ariga, K. Nanoporous Carbon Tubes from Fullerene Crystals as the π-Electron Carbon Source. *Angew. Chem. Int. Ed.* **2015**, *54*, 951–955. [CrossRef]

17. Tang, Q.; Bairi, P.; Shrestha, R.G.; Hill, J.P.; Ariga, K.; Zeng, H.; Ji, Q.; Shrestha, L.K. Quasi 2D Mesoporous Carbon Microbelts Derived from Fullerene Crystals as an Electrode Material for Electrochemical Supercapacitors. *ACS Appl. Mater. Interfaces* **2017**, *9*, 44458–44465. [CrossRef] [PubMed]

18. Bairi, P.; Shrestha, R.G.; Hill, J.P.; Nishimura, T.; Ariga, K.; Shrestha, L.K. Mesoporous Graphitic Carbon Microtubes Derived from Fullerene C_{70} Tubes as a High Performance Electrode Material for Advanced SuperCapacitors. *J. Mater. Chem. A* **2016**, *4*, 13899–13906. [CrossRef]

19. Benzigar, M.R.; Joseph, S.; Ilbeygi, H.; Park, D.-H.; Sarkar, S.; Chandra, G.; Umapathy, S.; Srinivasan, S.; Talapaneni, S.N.; Vinu, A. Highly Crystalline Mesoporous C_{60} with Ordered Pores: A Class of Nanomaterials for Energy Applications. *Angew. Chem. Int. Ed.* **2018**, *57*, 569–573. [CrossRef] [PubMed]

20. Benzigar, M.R.; Joseph, S.; Baskar, A.V.; Park, D.-H.; Chandra, G.; Umapathy, S.; Talapaneni, S.N.; Vinu, A. Ordered Mesoporous C_{70} with Highly Crystalline Pore Walls for Energy Applications. *Adv. Funct. Mater.* **2018**, *28*, 1803701–1803710. [CrossRef]

21. He, Z.; Wei, P.; Xu, T.; Han, J.; Gao, X.; Lu, X. Defect-rich N/S-co-doped Porous Hollow Carbon Nanospheres Derived from Fullerenes as Efficient Electrocatalysts for the Oxygen Reduction Reaction and Zn–air Batteries. *Mater. Chem. Front.* **2021**, *5*, 7873–7882. [CrossRef]

22. He, Z.; Wei, P.; Chen, N.; Han, J.; Lu, X. N,S-Co-Doped Porous Carbon Nanofiber Films Derived from Fullerenes (C60) as Efficient Electrocatalysts for Oxygen Reduction and a Zn–Air Battery. *Chem. Eur. J.* **2021**, *27*, 1423–1429. [CrossRef] [PubMed]

23. Guan, J.; Chen, X.; Wei, T.; Liu, F.; Wang, S.; Yang, Q.; Lu, Y.; Yang, S. Directly Bonded Hybrid of Graphene Nanoplatelets and Fullerene: Facile Solid-state Mechanochemical Synthesis and Application as Carbon-based Electrocatalyst for Oxygen Reduction Reaction. *J. Mater. Chem. A* **2015**, *3*, 4139–4146. [CrossRef]

24. Gao, R.; Dai, Q.; Du, F.; Yan, D.; Dai, L. C60-Adsorbed Single-Walled Carbon Nanotubes as Metal-Free, pH-Universal, and Multifunctional Catalysts for Oxygen Reduction, Oxygen Evolution, and Hydrogen Evolution. *J. Am. Chem. Soc.* **2019**, *141*, 11658–11666. [CrossRef]

25. Yang, J.; Heo, M.; Lee, H.J.; Park, S.-M.; Kim, J.Y.; Shin, H.S. Reduced Graphene Oxide (rGO)-Wrapped Fullerene (C_{60}) Wires. *ACS Nano* **2011**, *5*, 8365–8371. [CrossRef]

26. Hawkins, J.M.; Meyer, A.; Lewis, T.A.; Loren, S.; Hollander, F.J. Crystal Structure of Osmylated C60: Confirmation of the Soccer Ball Framework. *Science* **1991**, *252*, 312. [CrossRef]

27. Zheng, S.; Lu, X. Formation Kinetics and Photoelectrochemical Properties of Crystalline C_{70} One-dimensional Microstructures. *RSC Adv.* **2015**, *5*, 38202–38208. [CrossRef]

28. Huang, B.; Liu, Y.; Huang, X.; Xie, Z. Multiple Heteroatom-doped Few-layer Carbons for the Electrochemical Oxygen Reduction Reaction. *J. Mater. Chem. A* **2018**, *6*, 22277–22286. [CrossRef]

29. Bian, Y.; Wang, H.; Hu, J.; Liu, B.; Liu, D.; Dai, L. Nitrogen-rich Holey Graphene for Efficient Oxygen Reduction Reaction. *Carbon* **2020**, *162*, 66–73. [CrossRef]

30. Krishnamoorthy, K.; Veerapandian, M.; Yun, K.; Kim, S.J. The Chemical and Structural Analysis of Graphene Oxide with Different Degrees of Oxidation. *Carbon* **2013**, *53*, 38–49. [CrossRef]

31. Gao, J.; Wang, Y.; Wu, H.; Liu, X.; Wang, L.; Yu, Q.; Li, A.; Wang, H.; Song, C.; Gao, Z.; et al. Construction of a sp^3/sp^2 Carbon Interface in 3D N-Doped Nanocarbons for the Oxygen Reduction Reaction. *Angew. Chem. Int. Ed.* **2019**, *58*, 15089–15097. [CrossRef] [PubMed]